“This is an Accepted Manuscript of an article published by Taylor & Francis in Journal of Turbulence on 12 Sep 2021, available online: https://www.tandfonline.com/doi/full/10.1080/14685248.2021.1973015

Large-Eddy Simulations of the flow on an airfoil with leading-edge imperfections

Vishal Kumar[a], Ugo Piomelli[a] and Oriol Lehmkuhl[b]

[a]Queen's University, Kingston, Ontario, Canada; [b]Barcelona Supercomputing Centre, Barcelona, Spain

ARTICLE HISTORY
Compiled September 16, 2021

ABSTRACT
We performed large-eddy simulations of the flow over an airfoil to understand the effects of leading-edge roughness designed to mimic ice accretion. The roughness elements protrude outside the boundary layer, which, near the leading edge, is very thin; thus, the configuration does not represent a classical rough-wall boundary layer, but rather the flow over macroscopic obstacles. A grid convergence study is conducted and results are validated by comparison to numerical and experimental studies in the literature. The main effect of the obstacles is to accelerate transition to turbulence. Significant variations in structure generation are observed for different roughness shapes. The three-dimensionality of the irregularities has a strong impact on the flow: it creates alternating regions of high-speed ("peaks") and low-speed ("valleys") regions, a phenomenon termed "channelling". The valley regions resemble a decelerating boundary layer: they exhibit considerable wake and higher levels of Reynolds stresses. The peak regions, on the other hand, are more similar to an accelerating one. Implications of the channelling phenomenon on turbulence modelling are discussed.

KEYWORDS
Large-eddy simulations; airfoil; roughness; icing

1. Introduction

Maintaining laminar flow on aircraft can decrease the drag and fuel consumption significantly. Thus, much effort has been expended to design airfoils and engine nacelles in which the transition to turbulence is delayed. This has been particularly successful in the design of Natural Laminar Flow (NLF) nacelles [1, 2]; maintaining laminar flow, for instance, results in a 1-2% reduction in total drag, which in turn amounts to about 1-2% reduction in cruise fuel burn. One of the main causes of disruption of the laminar flow on an engine nacelle or a wing is the presence of surface imperfections; they can be due to manufacturing (gaps between metal plates, rivets etc.), or to natural phenomena such as ice formation.

Ice depositions have particularly negative effects in aeronautical applications, since they affect the lift as well as the drag. Thus, much research has been carried out in this area, focusing onto three questions: (1) what are the geometrical ice shapes encountered in practice? (2) what are the effects of these ice-shapes on the flow field?

CONTACT U. Piomelli. Email: ugo@queensu.ca

and, (3) what are the ways to control or prevent ice accretion? A complete review of icing research can be found in papers by Gent *et al.* [3] and Cebeci and Kafyeke [4]. The literature regarding the first two questions will be briefly reviewed here; (3) is outside the scope of the present study.

Past research into ice accumulation dealt mainly with the physics of accretion and the prediction of different ice-shapes. Early efforts were carried out, for example by NASA [5, 6], ONERA [7, 8] and the National Research Council (NRC) in Canada [9, 10]. Over the years, researchers have documented many different types of ice-shapes using both experimental measurements and numerical ice-accretion prediction models such as LEWICE [11, 12, 13, 14] and FENSAP-ICE [15, 16, 17].

The leading edge of an airfoil has been established to be the most sensitive region for ice formation [18, 19]. Cebeci [20, 21] found that the accumulation can resemble sand-grain roughness, or can be large-scale, and change the shape of the airfoil entirely. Lynch and Khodadoust [22] observed that both of these types of accumulations are highly dangerous and can cause performance degradation, in terms of maximum lift capability, up to 40%(for sandgrain-type accumulations) or 80% (for large-scale accretion). They classified these shapes based on the physical processes governing their formation and their topology. Bragg *et al.* [23] classified ice accretions into four major categories: ice roughness, horn ice, streamwise ice and spanwise-ridge ice, based on the difference in the flow-field observed. They also observed that many ice shapes do not belong to a single category, but may have features representative of two or more.

Ice roughness (which supplies the motivation for this study) occurs in the initial stages of the ice-accretion process, where each roughness element acts, more-or-less, as an isolated entity. Shin and co-workers [24, 25, 26, 27] performed experiments on a NACA 0012 airfoil, and found ice roughness to have a height greater than the local boundary layer thickness, even in the early stages of the ice-accretion process. They further described the geometrical features of ice roughness, which has an effectively smooth zone sandwiched between two rough patches (one on each side of the airfoil). McClain and co-workers [28, 29, 30, 31] made detailed measurements of the ice-roughness topology on a NACA 0012 airfoil at 0° angle of attack and showed that the surface topology varies significantly, from a primarily 3D accumulation to a more 2D character, with accumulation time.

Most experimental work on the effect of ice roughness on airfoils and wings have tried to quantify the degradation of the aerodynamic performance. The general consensus is that these accretions result in an increased drag [22] and reduction in lift [32, 33]. Some studies, however, have observed an increase [34, 35, 36] in lift where, they note, the roughness effectively acts as leading edge slat. More detailed studies have focused on other aspects, such as the changes in the transition process [37, 38, 39], the effect of size [40, 41], shape [42, 43, 21], location [44, 45] and density [21, 46] of the roughness elements.

Kerho and Bragg [37] observed that roughness triggers the transition process at (or very near) the roughness trailing-edge through a markedly different route than on smooth airfoils. Plogmann *et al.* [39] conducted experiments on a single hemispherical roughness element on the leading edge and found that flow transitions only when $h/\delta > 0.75$, where h is the roughness height and δ the local boundary layer thickness; for $h/\delta < 0.2$ they did not observe any noticeable mean velocity distortion. Zhang *et al.* [40, 41] found roughness height to be a more significant factor in low-Re flow degradation than the distribution pattern (aligned *vs.* staggered elements). More recently, Vinnes *et al.* [47] conducted experiments to demonstrate the feasibility of reduced-order modelling for flow over iced airfoils.

Numerical studies on the flow over rough airfoils have been carried out mostly using the Reynolds-Averaged Navier-Stokes (RANS) approach and, more recently, hybrid methods that solve the Reynolds-Averaged Navier-Stokes (RANS) equations near the wall, switching to large-eddy simulations (LES) away from the solid surfaces. Hybrid RANS-LES methods will be referred to as HRL. Due to the scale and simplicity of the geometry and its strong effects on aerodynamics, most studies have focused on the horn type of roughness. Brown *et al.* [48] performed resolved-calculations using the implicit LES (ILES) approach and found the results to be accurate until the pre-stall regime; ILES fails to predict the unsteadiness of the flow at higher angles of attack. They also found a strong effect (with a variance of 95%) of the spanwise variation in the geometry on lift coefficients for angle of attack in the range $5^o - 15^o$.

In a recent review paper, Stebbins *et al.* [49] made a comprehensive assessment of RANS [50, 51, 52] and HRL methods [53, 54, 55] in the study of horn geometry and concluded that the results of HRL methods are more accurate than RANS solutions, particularly at high angles of attack, owing to the ability of LES-based methods to capture the unsteadiness of the flow. Still, they displayed discrepancies with the experimental data. Xiao *et al.* [56] used wall-modelled LES (WMLES) and observed better predictions of the separated shear-layer dynamics.

Studies related to ice-roughness geometry are fewer. In their review, Stebbins *et al.* [49] mention no study of ice roughness that uses eddy-resolving methods. Konig *et al.* [57] and Ribeiro *et al.* [58] performed Very Large Eddy Simulations (VLES) combined with a Lattice-Boltzmann method, on ice-roughness geometries with height $\sim 0.2\%$ of the chord. While Konig *et al.* [57] noted an over-prediction of the maximum lift, Ribeiro *et al.* [58] observed that the use of simplified shapes that are spanwise constant is not realistic because of the three-dimensional flow field due to an uneven separation pattern behind the roughness. Recently, Ribeiro *et al.* [59, 60] reported a DNS study of a NACA 0012 airfoil, at $Re = 657,000$ and angle of attack of 0^o, with sand-grain variety of roughness on the leading edge ($x/c < 20\%$) using a Lattice-Boltzman method, within the context of noise prediction; a detailed flow analysis was not performed. Moreover, although they mentioned the grid to have a uniform distribution of $y^+ = 0.5$ on the airfoil surface, a proper grid-convergence study was not reported.

To understand better how ice formations affect the transition to turbulence on airfoils and nacelles, and how the turbulent flow is modified, we carried out a study of the flow over a NACA 4412 airfoil at small angle of attack ($\alpha = 5^\circ$) and moderate Reynolds number ($Re = 200,000$). The leading edge is modified by adding either two-dimensional trip wires, or three-dimensional protuberances similar to those observed in the ice-accretion experiments of McClain *et al.* [29]. We use Wall-Resolved LES (WRLES), which allow us to study the unsteadiness and three-dimensionality of the flow in great detail. In our simulations, most of the turbulent scales are resolved everywhere (even near the roughness) which is an advantage over RANS and HRL methods, since the model for the unresolved scales has a less significant effect on the results, and the flow near the roughness elements can be studied. It should be remarked that, although we sometimes refer to the irregularities as "roughness", they are much larger than is usual in rough-wall studies. Since they are placed at the leading edge, where the boundary layer is very thin, they protrude out of the boundary layer itself. Thus, we are considering the boundary-layer flow over large obstacles, rather than a classical rough-wall boundary layer.

In the following we will first formulate the problem, in terms of numerical method, physical model and geometric configuration. Then we will validate the simulations and present the results. Finally, comments and recommendations for future work will conclude the paper.

2. Problem formulation and methodology

2.1. Governing equations

The flow over a NACA 4412 airfoil at $Re = U_o c/\nu = 200,000$ (based on freestream velocity U_o and chord c) and angle-of-attack $\alpha = 5^o$ was studied using Wall-Resolved Large-Eddy Simulations (WRLES). The filtered Navier-Stokes equations for incompressible flow were solved:

$$\frac{\partial \overline{u}_i}{\partial x_i} = 0. \tag{1}$$

$$\frac{\partial \overline{u}_i}{\partial t} + \frac{\partial}{\partial x_j}\left(\overline{u}_i \overline{u}_j\right) = -\frac{1}{\rho}\frac{\partial \overline{p}}{\partial x_i} - \frac{\partial \tau_{ij}}{\partial x_j} + \nu \frac{\partial^2 \overline{u}_i}{\partial x_j \partial x_j}. \tag{2}$$

where $\tau_{ij} = \overline{u_i u_j} - \overline{u}_i \overline{u}_j$ are the unresolved Sub-Filter Scale (SFS) stresses, $x,\ y,\ z$ (or $x_1,\ x_2,\ x_3$) are the streamwise, vertical and spanwise directions, respectively. The corresponding filtered instantaneous pressure and velocity fields are $\overline{p}$ and $\overline{u},\ \overline{v},\ \overline{w}$ (or $\overline{u}_i$). We will also be using subscripts t and n to indicate the velocity components tangential and normal to the airfoil surface. In the following, the overline will be dropped; u_i and p will be implicitly assumed to be filtered quantities.

The unresolved, subfilter-scale, stresses are modelled using the ILSA model [61], in its local formulation [62]. The model parameter, s_τ, which measures the SFS contribution to the dissipation, is set to 0.1 based on the recommendation of Lehmkuhl *et al.* [63] for prismatic elements.

The simulations in this study are performed using Alya, a multi-physics, massively parallelized, unstructured finite-element simulation code developed at Barcelona Supercomputing Center [64, 65]. It has been widely validated in many turbulent-flow configurations: [66, 67, 68, 69, 63, 70]. The governing equations (1) and (2) are discretised on a collocated unstructured grid by means of low dissipation second-order conservative schemes [71]. The same interpolation scheme for velocity (u_i) and pressure (p) is used in space. A third order Runge-Kutta explicit time discretization is used to advance the solution in time, combined with an eigenvalue-based time-step estimator [72]. A fractional time-step algorithm is used to solve the resulting system of linear equations [73]. The Poisson equation is solved using a Deflated Conjugate Gradient[74]; convergence and stopping criteria are based on the lagged algebraic residual.

2.2. Airfoil geometries

Four surface geometries (shown in Figure 1) were studied. They are all based on the NACA 4412 airfoil, with various leading-edge modifications. In addition to the unmodified airfoil with a smooth leading-edge (SLE), we considered a Tripped Boundary-Layer (TBL) case with three cylindrical elements near the leading edge on the suction side, and two Rough Leading-Edge cases (RLE1 and RLE2) with randomly distributed roughness elements.

The three semi-cylindrical trips in the TBL geometry were located at 0.1%, 2.1% and 4.2% of the chord c; their heights were $0.003\,c$ (see Figure 1(b)). The size and location of the trips was chosen to achieve early establishment of the turbulent flow regime. The

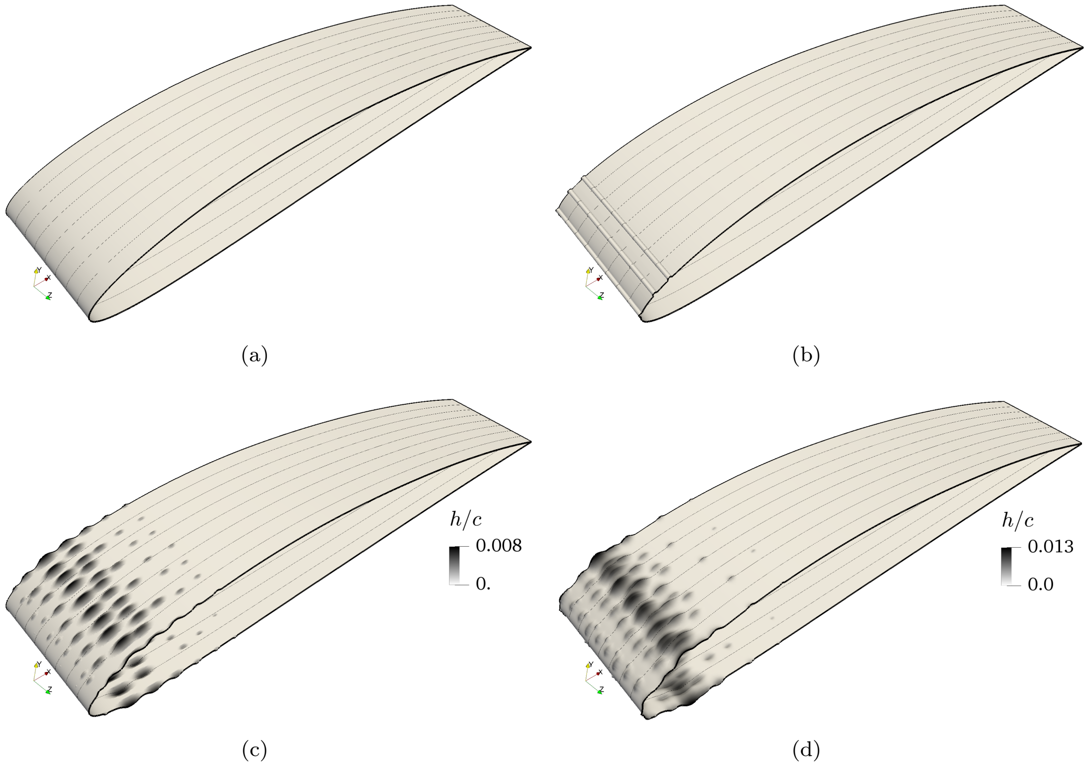

Figure 1. NACA4412 airfoil geometries used in the present study: (a) Smooth Leading Edge (SLE); (b) Tripped Boundary Layer (TBL); (c) Rough Leading Edge 1 (RLE1); (c) Rough Leading Edge 2 (RLE2)

RLE1 and RLE2 cases try to reproduce the ice accretions in the study by McClain *et al.* [31] (see Figure 3 in that paper). The roughness elements were ellipsoids; their height, h, depended on their x location, to have a similar distribution as in the study by McClain *et al.* [31]. The maximum peak-height, $h_{p,\max}$, was $0.008\,c$ and $0.013\,c$ for the RLE1 and RLE2 cases, respectively. The corresponding mean peak-roughness height, $\overline{h}_p$, was $0.004\,c$ and $0.009\,c$. Since the roughness elements were located close to the leading edge, where the boundary layer is very thin, they extend outside the boundary layer; for example, in TBL the ratio of roughness height to the local boundary-layer thickness are 23, 2 and 1 respectively for the three semi-cylindrical trips used.

Although care was taken for these geometries to resemble those found in the experiments of McClain *et al.* [31], some simplification was required to maintain grid quality. The spacing between the elements, for instance, is nearly constant, with a small random variation, and their shape is ellipsoidal. The ice deposition, as shown by [31], has a more random distribution. By matching the height distribution and length scale of the real ice roughness, however, we retained key elements of an real geometry to be able to improve the understanding of the flow physics involved.

2.3. Computational domain and boundary conditions

All computations were carried out on a $40c \times 40c \times 0.2c$ domain (shown in Figure 2), with the leading edge placed at the origin. This is consistent with the previous simulations carried out by [75, 76] who used the same methodology to study the flow over a NACA 0012 airfoil. The two-point correlation of the velocity components in the

Case	N_z	Δs^+	Δn^+	Δz^+	$N_{dof} \times 10^{-6}$	C_l	C_d
SLE	97	2.8	2.8	18	14.1	0.95	0.0176
TBL - C	97	4.3	4.3	20	8.1	0.84	0.0239
TBL - M	145	1.52	1.52	13	28.8	0.81	0.0244
TBL - F	197	0.85	0.85	10	80.5	0.80	0.0248
RLE1	145	1.8	1.8	14.5	28.3	0.77	0.0267
RLE2	145	1.8	1.8	14.5	28.3	0.77	0.0327
Smooth, Ref. [78]	-	18	0.64	9	336	0.885	0.0185

Table 1. Summary of computational parameters. The grid spacing in viscous units (denoted by +) is calculated at $x/c = 0.6$ on the suction side of the airfoil. C, M and F refer to Coarse, Medium, and Fine meshes. N_z: number of points in the spanwise direction; Δs, Δn: grid spacing in wall-parallel and wall-normal directions; N_{dof}: number of degree of freedom per unknown. C_l, C_d are the lift and drag coefficients.

spanwise direction (not shown) confirmed that the domain is wide enough to contain all the important structures. An open-source grid generation tool, Gmsh [77], was used to generate the mesh. A body-fitted grid with triangular-prism elements was used. Mesh smoothing was used in all directions to maintain a good quality of the final grid used. A sample grid used in this study is shown in Figure 2; an uniform element-size is used on the airfoil surface and grid is stretched as we move away from the body.

The boundaries used the following conditions: at the inlet a uniform velocity $(u, v, w) \equiv (U_o \cos\alpha, U_o \sin\alpha, 0)$ was assigned; at the outlet, a pressure-based condition was applied, where the total pressure (p_d) and outlet normal velocity (u_n) are related as $p_d = {}^1\!/\!{}_2 \rho u_n^2$. No-slip conditions were imposed on the airfoil surface, and the flow was assumed to be periodic in the spanwise direction. Since no disturbances were introduced artificially, the flow transitions naturally from the amplification of small perturbations (due to round-off or truncation error). As will be shown, the presence of leading-edge imperfections plays a critical role in the transition process.

Parameters related to the mesh are listed in Table 1, along with the lift (C_l) and drag (C_d) coefficients. They are defined as:

$$C_l = \frac{2\mathcal{L}}{\rho U_o^2 z_D c}; \quad C_d = \frac{2\mathcal{D}}{\rho U_o^2 z_D c}; \tag{3}$$

where $\mathcal{L}$ and $\mathcal{D}$ are the lift and drag forces calculated as the sum of pressure and viscous contributions at each computational cell on the airfoil surface.

2.4. Averaging operators

In studies of the flow over airfoils it is customary to average the turbulent quantities in both time and the spanwise direction, in which the flow is statistically homogeneous. Here, in the RLE1 and RLE2 cases, the three-dimensional nature of the roughness introduces spanwise inhomogeneities that persist along the airfoil (as will be shown momentarily). It is convenient, then, to introduce two averaging operators, similar to the triple decomposition commonly used to study flows over rough surfaces [79, 80].

In addition to the standard time-averaging (indicated by an overbar or by a capital letter: $\overline{f} = F$), we can also average quantities both in time and in the spanwise direction

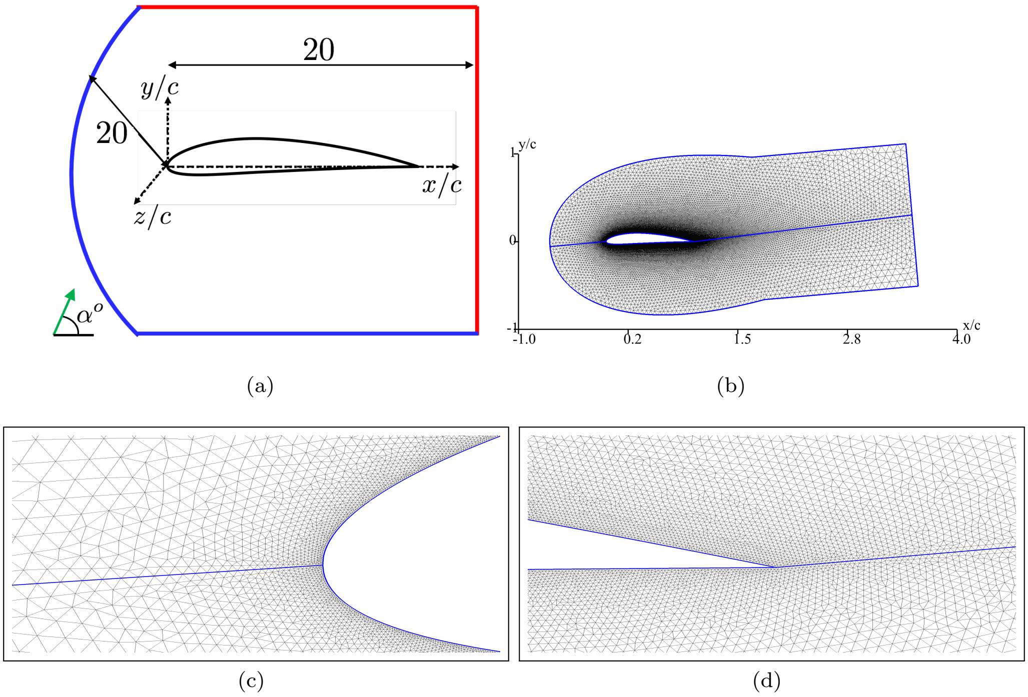

Figure 2. A sample grid distribution; actual grid densities for different cases are reported in Table 1. (a) Sketch (not to scale) showing the computational domain, blue represents inflow and red represents outflow conditions; (b) grid distribution near the airfoil; (c) enlargement of the leading edge, and (d) of the trailing edge.

("double-averaged", or "DA", quantities); the spanwise averaging is indicated by angle brackets, so that a DA quantity would be written as $\langle F \rangle = \langle \overline{f} \rangle$. Note that if the flow is statistically homogeneous, time-averaging, spanwise averaging and double averaging give the same result. A turbulent quantity can be decomposed in various ways:

$$f = F + f' = \langle F \rangle + \widetilde{f} + f' = \langle F \rangle + f''. \tag{4}$$

$\widetilde{f}$ is known as the "wake field," or "form-induced perturbation." It represents the deviation of the time-averaged field from the time-and-space averaged one, and highlights the geometry-induced effects. The wake field is stationary, and its spanwise average is zero. f' is the stochastic fluctuations. f'' is the deviation from the DA quantity, which contains a steady component, $\widetilde{f}$, as well as the fluctuation f'.

When we apply the triple decomposition to the velocity and calculate the DA second-order moments, we obtain:

$$\langle \overline{u_i u_j} \rangle = \langle U_i \rangle \langle U_j \rangle + \langle \widetilde{u}_i \widetilde{u}_j \rangle + \langle \overline{u_i' u_j'} \rangle \tag{5}$$

$\widetilde{u}_i \widetilde{u}_j$ are the "dispersive stresses", $\overline{u_i' u_j'}$ the stochastic ones. If the flow is homogeneous in z, as well as far from the roughness elements, the dispersive stresses vanish.

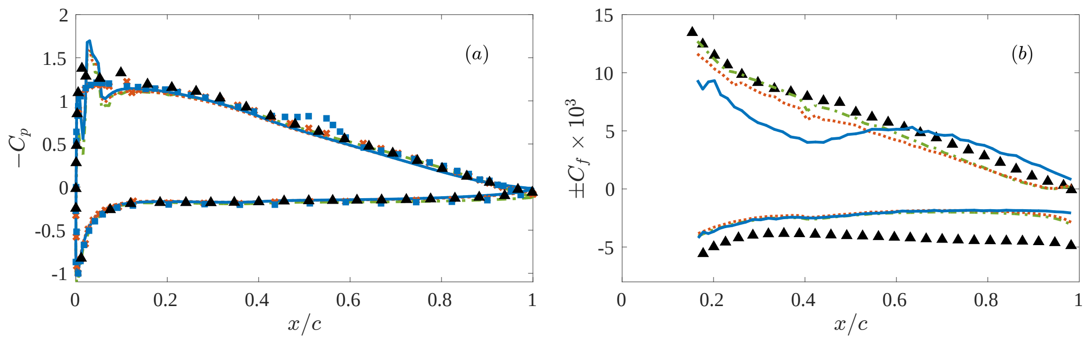

Figure 3. Grid convergence study for the Tripped Boundary Layer (TBL) case: (a) Pressure (C_p); and (b) Friction (C_f) coefficients. ▬ Coarse; ⋯ Medium; - - Fine; ▲ LES [78]; × Exp., tripped [81]; ■ Exp., smooth [81]. For clarity, C_f is plotted on the suction side, $-C_f$ on the pressure side.

3. Results

3.1. Grid-refinement study

We performed a grid-refinement study, using the TBL configuration. The three grid resolutions used were reported in Table 1, where they are denoted by TBL-C, TBL-M and TBL-F for the coarse, medium and fine meshes, respectively.

The pressure (C_p) and skin-friction (C_f) coefficients, are defined as

$$C_p = \frac{2(\langle P \rangle - p_\infty)}{\rho U_o^2}; \quad C_f = \frac{2\langle \overline{\tau}_w \rangle}{\rho U_o^2} \tag{6}$$

where p_∞ is the reference pressure, and τ_w is the wall shear-stress respectively. The pressure coefficient is fairly insensitive to grid resolution in the smooth part of the airfoil and all grids give similar results. C_f is more sensitive to the grid size; the medium and fine meshes are in good agreement with each other. Both C_f and C_p agree well with the reference data.

Figure 4 shows profiles of the mean wall-parallel velocity U_t and turbulent kinetic energy (TKE), $\mathcal{K} = \overline{u_i' u_i'}/2$. Both U_t and $\mathcal{K}$ are also spanwise-averaged, and normalized by the edge velocity U_e (which will be defined momentarily). The coloured area represents error bars for the medium grid. The error is calculated as

$$\epsilon = \frac{f_2 - f_1}{f_1(r^p - 1)} \tag{7}$$

where f_1 represents the quantity considered (velocity or TKE) on the fine grid, f_2 the same on the medium grid, $r = 3^{1/3}$ is the grid refinement ratio, and $p = 2$ is the order of accuracy of the spatial scheme used. The factor $(r^p - 1)$ in the denominator serves to avoid underestimation of the error when the grid is refined by small amounts (i.e., $r \simeq 1$). While the mean velocity is grid-converged, the difference in the TKE between medium and fine grid is significant, especially near the trailing edge. Similar observations on the grid convergence were made by Vinuesa *et al.* [78] in their study of Reynolds number effects on flow over NACA 4412 airfoil at $Re = 1 \times 10^6$ with a coarser grid resolution. Since the mean velocity is grid-converged on the medium grid, while the TKE matches at least the general behaviour, the medium grid is considered sufficient to resolve the main phenomena discussed hereafter, with the *caveat* that any

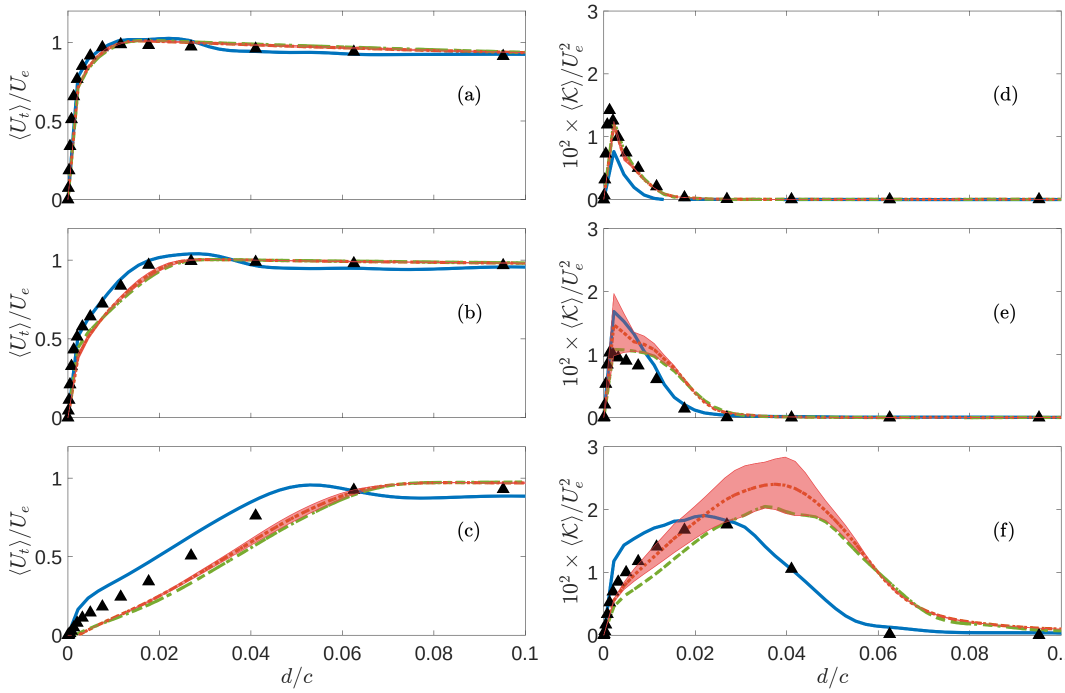

Figure 4. Grid convergence study for the Tripped Boundary Layer (TBL) case: (a,b,c) wall-parallel velocity ($\langle U_t \rangle / U_e$); (d,e,f) Turbulent Kinetic Energy ($10 \times \langle \mathcal{K} \rangle / U_e^2$) at specific streamwise locations, (a,d) $x/c = 0.2$; (b,e) $x/c = 0.58$ and (c,f) $x/c = 0.98$ respectively; d is the wall-normal distance; U_e is the velocity at the boundary layer edge. Coarse; Medium; Fine; ▲ LES [78].

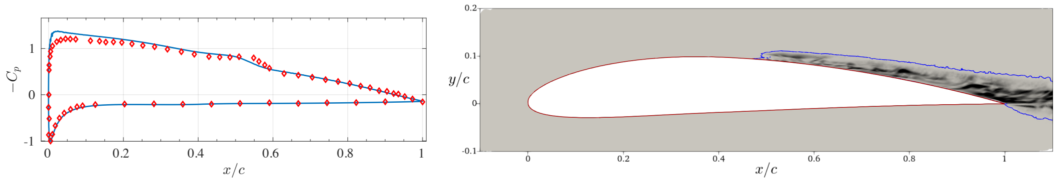

Figure 5. (a) Pressure coefficient for the SLE case, medium grid. Line: present results; symbols [81]. (b) Instantaneous SFS eddy-viscosity ν_t (normalized by the molecular viscosity) in an $xy-$ plane. Colours range from 0 (white) to 10 (black); the solid blue line is the $\nu_t/\nu = 0.1$ contour.

conclusion regarding the TKE can only be qualitative. Although the fine resolution would be optimal, its computational requirements did not make it possible to use it for all cases. A typical simulation on the medium grid required around 7.2 million CPU hours on the Compute/Calcul Canada systems.

Finally, in Figure 5(a) we compare the pressure coefficient for the SLE case with the experimental data of Mallor [81], who carried out measurements for this airfoil at the same flow configuration. Measurements were taken for a case in which the boundary layer was tripped, and for an untripped one. Only the C_p is available for the untripped case corresponding to SLE. The agreement of the simulation with the experimental data is very good. In particular, we note that the onset of transition results in a kink in the pressure-coefficient profile at $x/c \simeq 0.55$, which is captured well by the simulation. We also note that the ILSA model has the property that ν_t vanishes in laminar regions of the flow; this behaviour is observed here, Figure 5(b). Thus, the prediction of transition is only affected by the grid resolution and not by the SFS model.

A point that requires further discussion regards the differences observed in Figure 4 between the present results and the data by Vinuesa *et al.* [78], who studied the same airfoil, at the same Reynolds number and angle of attack. The flow in this configuration has been shown to be very sensitive to the laminar/turbulent transition process, i.e., to the tripping device used [82, 83]. Vinuesa *et al.* [78] tripped the boundary layer, on both sides of the airfoil, using volumetric forcing at $x/c = 0.1$ (see [83] for details). In our study, on the other hand, we use localized perturbations (the trip wires for case TBL, the roughness for RLE1 and RLE2), which cause significantly different routes to turbulence. Recently, in fact, Tanarro *et al.* [84] extended the work of Vinuesa *et al.* [78] to enable Adaptive Mesh Refinement (AMR) for the simulations of the NACA 4412 airfoil. Although they used the same code and numerical setup as [78], with a minimal change in the tripping method, they still observed differences in the flow field, both on the suction and on the pressure sides. Given this sensitivity of boundary layer to the tripping methodology used, perfect quantitative agreement between the current study and the data of [78] could not be achieved, and should not be expected. For a case in which the tripping is not present, however, we obtain better agreement. We rely, instead, on the level of grid convergence achieved, on the fact that the computational methodology has been thoroughly validated for different flows of this type [75, 85, 63, 70], in terms of both numerical scheme and SFS model, and on the good agreement with a case in which the flow was untripped, discussed earlier.

3.2. Instantaneous flow structures

Figures 6 and 7 show the iso-surfaces of the second invariant of the velocity-gradient tensor,

$$Q \equiv \frac{1}{2}\left(|\mathbf{\Omega}|^2 - |\mathbf{S}|^2\right) \tag{8}$$

where $\mathbf{\Omega}$ and $\mathbf{S}$ are the rotation and rate-of-strain tensors. All quantities are normalized by U_o and c.

In the SLE case the boundary layer on the suction side, is initially laminar; the flow separates at $x/c = 0.41$ and reattaches at $x/c = 0.53$ creating a thin, closed laminar separation bubble with a maximum height of $0.005c$. The flow then undergoes a transition process that appears to be associated with undulations of the spanwise vortices formed in the separated shear-layer. The flow breaks down shortly after the formation of these secondary instabilities, re-attaches and finally develops into Λ-shaped vortices.

In the TBL case the flow is significantly different; spanwise vortices are formed in the shear layer emanating from the top of the first semi-cylindrical element (marked as *T1* in Figure 6(b)), which are advected downstream. The flow remains coherent for the first 20-30% of the chord (region **A** in the Figure), but then the 3D perturbations break the coherence of the spanwise vortices, and horseshoe vortices appear (region **B**). The flow becomes turbulent much earlier than in the SLE case due to the formation and breakdown of the rollers.

In the RLE1 case, we observe an early formation of 3D structures, which coalesce into hairpin-like vortices downstream of the roughness, in the region marked **B** in Figure 6(c). An interesting feature of this flow is the alignment of the hairpins (in the region marked as **A**, for instance). The alignment is associated with a channelling phenomenon that will be discussed momentarily. Eventually, the structures become

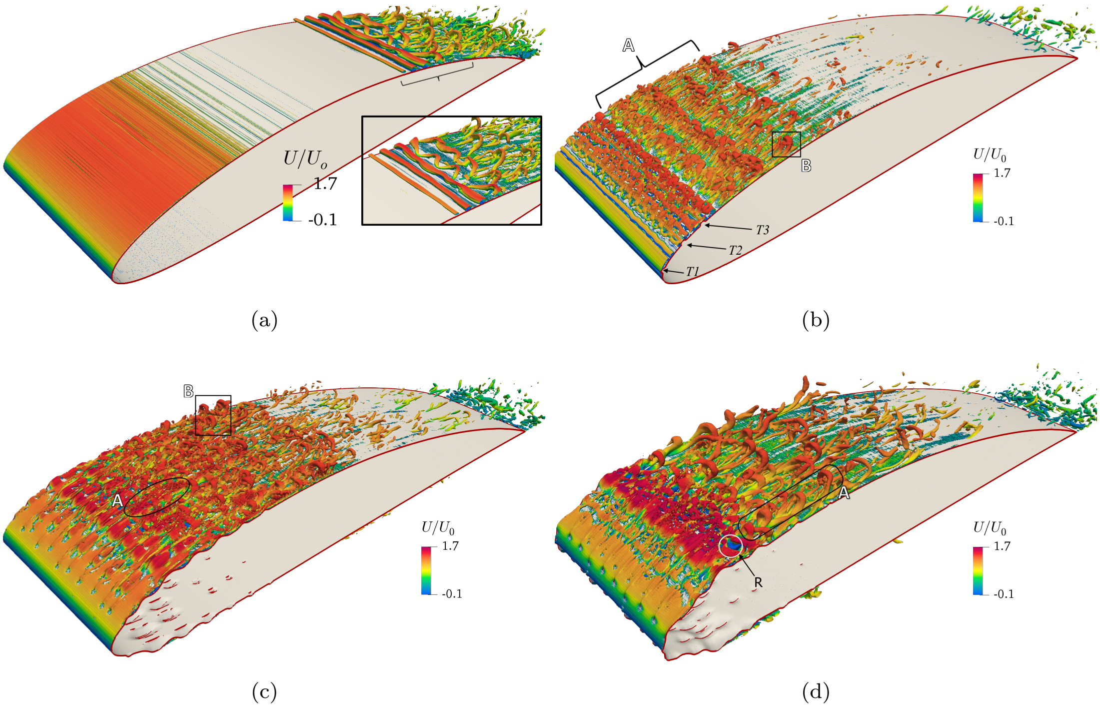

Figure 6. Iso-surfaces of $Q = 750U_o^2/c^2$, coloured by the time-averaged streamwise velocity U/U_o, for (a) SLE case; (b) TBL case; (c) RLE1 case; (d) RLE2 case. A top view of the region marked by curly braces in the SLE case is shown in the inset. The locations of the trips in TBL case are shown by arrows and marked with $T1$, $T2$ and $T3$.

larger and lose their alignment, and a more random distribution is observed. In the adverse pressure-gradient region the vortices are less coherent and less frequent.

For the RLE2 case, quasi-2D vortex-shedding from the obstacles is visible (for example, in region **A** in Figure 6(d)); the shed vortices become elongated downstream due to the shear. The turbulent structures are significantly larger than in the other cases, reflecting the greater height of the imperfections.

Since in the SLE and TBL cases the surface on the lower side is smooth and the pressure gradient is favourable the boundary layer there remains laminar. The instantaneous structures for the RLE1 and RLE2 cases are shown in Figure 7. The mechanism of flow breakdown is quite different for the two cases; while the flow in the RLE2 case undergoes transition soon after encountering the roughness elements, quasi-laminar regions can be observed in the wake of the smaller elements (regions that will be termed "valley regions").

The instantaneous fields are useful to understand the general features of the flow. In the following, a quantitative analysis will be carried out for the boundary layer parameters and the three-dimensional effect of the leading-edge obstacles on the mean flow.

3.3. Boundary-layer behaviour

There are various criteria in the literature for finding the edge of the boundary layer in turbulent flows; among them is the use of composite profiles [86, 87], or of an intermittency factor [88], the spanwise-vorticity approach ([89]), the modified diagnostic-plot

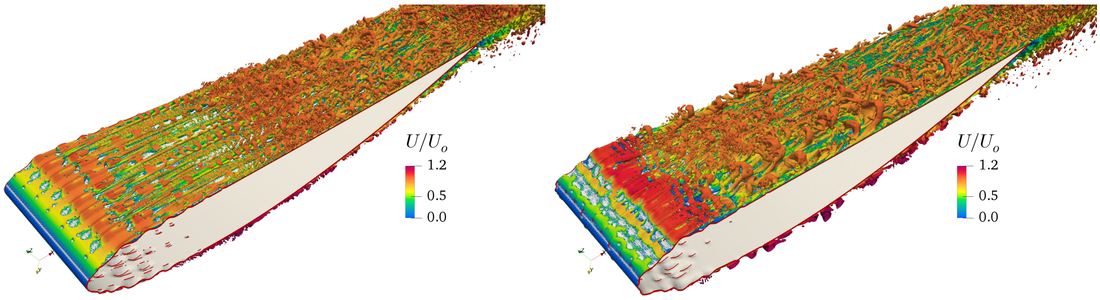

(a) (b)

Figure 7. Iso-surfaces of $Q = 50U_o^2/c^2$, coloured by the time-averaged streamwise velocity U/U_o, for (a) RLE1 case; (b) RLE2 case on the pressure side.

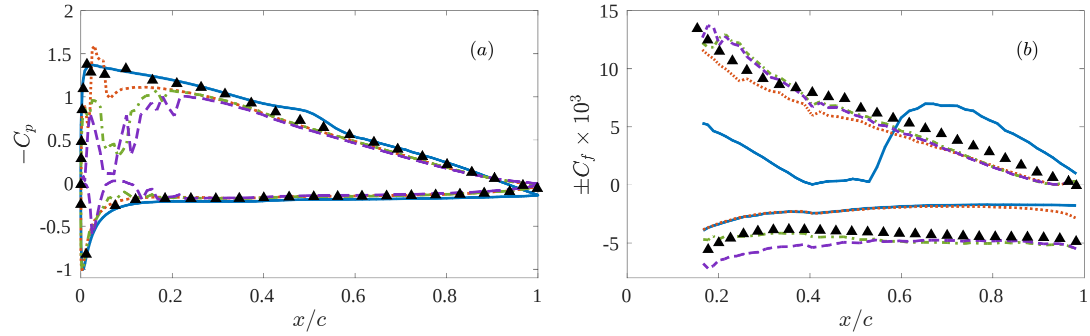

Figure 8. (a) Pressure coefficient; (b) Friction coefficient. — SLE; ···· TBL; -·-· RLE1; - - - RLE2; ▲ LES [78]. For clarity, C_f is plotted on the suction side, $-C_f$ on the pressure side.

concept [90] and the method proposed by Griffin *et al.* [91] in which they fit a theoretical inviscid velocity profile (U_I) to the actual viscous one, and the edge of the boundary layer (i.e., the location where the velocity is $n/100$ of the edge velocity) is defined as the wall-normal location where $\langle U \rangle / U_I = n/100$. We have applied both Griffin's and diagnostic-plot criteria. On the suction side they give nearly identical results; on the pressure side the diagnostic-plot is harder to apply since the flow is laminar in the SLE and TBL cases. Therefore, only the results obtained using Griffin's criterion will be shown.

Figure 8 shows the pressure (C_p) and friction coefficients (C_f) on the airfoil. Once turbulence is established the surface-pressure distribution shows minimal variations among all cases, indicating the insensitivity of the outer, inviscid, flow to the boundary-layer behaviour at moderate and high Reynolds numbers; this is confirmed by the lift coefficient, Table 1; all the rough cases are within 1% of each other.

The C_f distribution, on the other hand, is quite sensitive to upstream conditions and to the tripping mechanism. On the suction side, SLE shows a typical transitional boundary-layer behaviour, with an overshoot of C_f above the turbulent values. Very small differences can be observed between the three rough cases: the TBL has a slightly lower friction; all cases agree reasonably well with the results of [78]. On the pressure side, the SLE and TBL cases have lower friction, since the flow is laminar. RLE2 has higher skin-friction than RLE1 immediately after the roughness; only for $x/c \geq 0.7$ the results of the two rough cases collapse (and also agree with the data by [78]). This difference can be due to several factors: one is the larger roughness elements in the RLE2 case, which cause a stronger disruption of the flow. The generation, in case RLE1, of streamwise vortices that alter the mean flow (which will be discussed later) may also play a role.

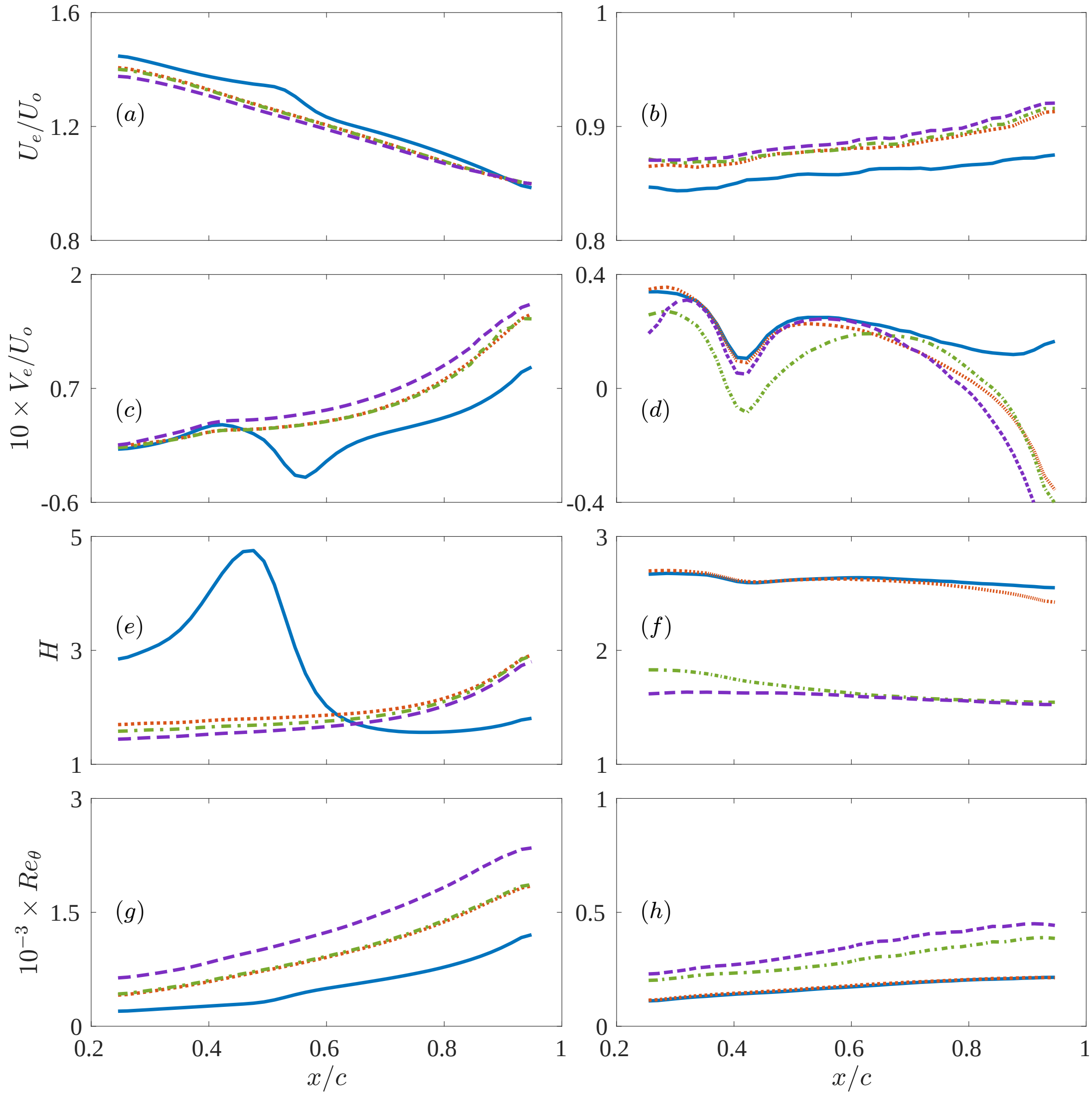

Figure 9. Boundary-layer parameters: *(a,b)* Wall-parallel edge velocity, U_e/U_o; *(c,d)* wall-normal edge velocity, V_e/U_o; *(e,f)* shape factor, H; *(g,h)* momentum-thickness Reynolds number, Re_θ. Suction side: *(a,c,e,g)*; pressure side: *(b,d,f,h)*. SLE; TBL; RLE1; RLE2.

Figure 9 shows the streamwise distribution of various boundary-layer parameters: only the flow downstream of the roughness is plotted. All quantities are calculated using double-averaged data. The streamwise and wall-normal edge velocities (U_e and V_e), the shape factor $H = \delta^*/\theta$, and momentum-thickness Reynolds number ($Re_\theta = U_e\theta/\nu$) are shown. The momentum and displacement thicknesses are defined as:

$$\delta^* = \int_o^\infty \left(1 - \frac{\langle U \rangle}{U_e}\right) dy \quad \theta = \int_o^\infty \frac{\langle U \rangle}{U_e}\left(1 - \frac{\langle U \rangle}{U_e}\right) dy. \tag{9}$$

The velocity at the edge of the boundary layer shows very little difference in the rough cases; the small bulge at $x/c \approx 0.5$ on the suction side for the SLE case is due to the laminar separation bubble. The boundary layer is considerably thicker when the flow is turbulent (cases TBL, RLE1 and RLE2 on the suction side, RLE1 and RLE2 only on the pressure side). This is reflected both in the larger magnitude of wall-normal velocity at the boundary-layer edge and in the momentum-thickness Reynolds number. It also confirms the visual impression from Figures 6 and 7. The boundary layer in case RLE2, in which the roughness elements are taller and the turbulent structures appeared larger, is the thickest. On the suction side the shape factor is affected by the recirculation bubble in case SLE; it is very similar in the other cases. Note that immediately after the roughness $H \simeq 1.6$ (close to the flat-plate turbulent boundary-layer value) in all cases in which the flow is turbulent; H increases in the adverse pressure-gradient (APG) region on the suction side, while remains nearly constant in the favourable pressure-gradient (FPG) region on the pressure side. There, $H \simeq 2.6$ (the laminar flat-plate value) when the flow remains laminar.

3.4. Double-averaged velocity

Figures 10 and 11 show the double-averaged velocity-component tangent to the wall, $\langle U_t \rangle$. Double-averaged statistics were collected for more than 100 LETOTs δ^*/u_τ (where δ^* and u_τ are calculated at $x/c = 0.6$ on the suction side) and then averaged in the spanwise direction.

On the suction side all the cases except SLE are turbulent from the first location onward. In fact, between $x/c \simeq 0.3$ and 0.7 they are very close to the standard logarithmic law, shown in Figure 11*(a,b)*. Here wall units, denoted by a +, are calculated using the local value of u_τ. Further downstream APG effects become significant and the velocity profile goes above the logarithmic law. In the rough cases the momentum deficit is larger than in the smooth one: the leading-edge protrusions act as flow obstacles and, in some cases, cause local flow separation. Although their roughness height, location and topology are different, the TBL and RLE1 cases have quite similar profiles at all locations. The SLE case has an altogether different behaviour: the flow is initially laminar (and the boundary layer is significantly thinner than in the other cases, Figure 10); an inflectional velocity then develops, and a recirculation region is formed. The flow then reattaches and a fuller velocity profile is established that tends towards an equilibrium turbulent boundary layer.

On the pressure side the SLE and TBL cases have laminar profiles at all locations. RLE1 and RLE2 cases, however, are turbulent and have similar profiles, following the logarithmic law. The dimensionless pressure gradient $K = (\nu/U_e^2)(dU_e/dx)$ is of order 10^{-7}, low enough that the slope of the logarithmic region is not altered very much. Only close to the roughness one can observe some difference between the two cases, RLE2 being closer to an equilibrium turbulent boundary layer. Possible causes for this difference will be discussed in the following.

3.5. Time-averaged statistics

The roughness elements near the leading edge in the TBL, RLE1 and RLE2 cases act as flow obstacles. Depending upon their placement, shape and distribution, they cause flow three-dimensionality and transition to turbulence, as discussed in Section 3.2. In the TBL case, on the suction side an initially 2D structure characterized by large spanwise-oriented vortices is followed by vortex breakdown and formation of hairpin-

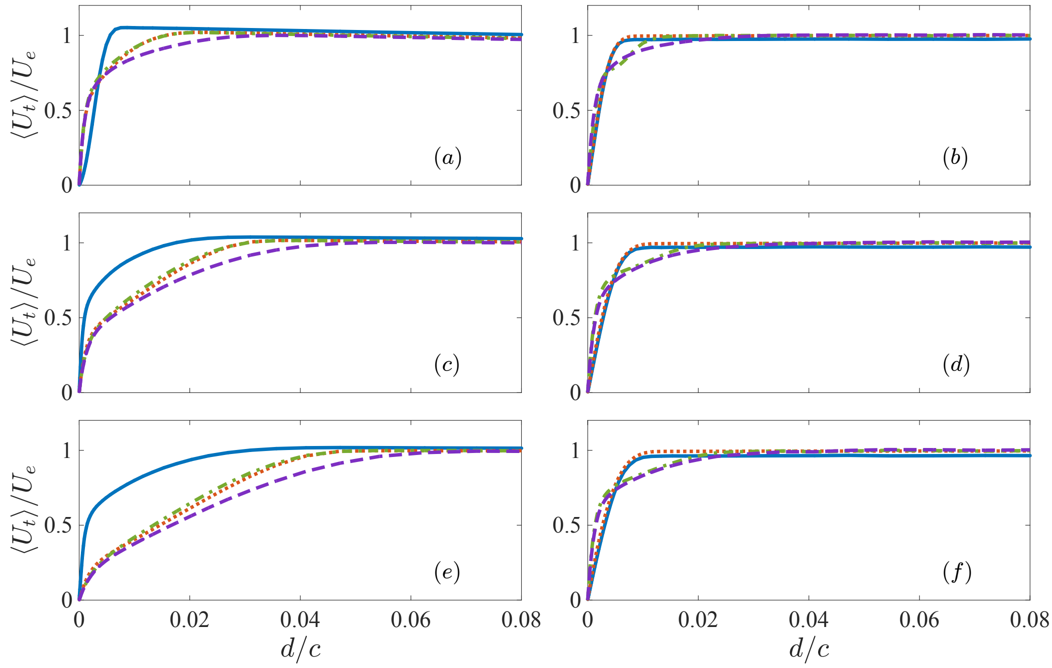

Figure 10. Wall-parallel velocity profiles. $(a, b) : x/c = 0.35$, $(c, d) : x/c = 0.67$, $(e, f) : x/c = 0.82$. (a, c, e) Suction side; (b, d, f) pressure side. SLE; TBL; RLE1; RLE2.

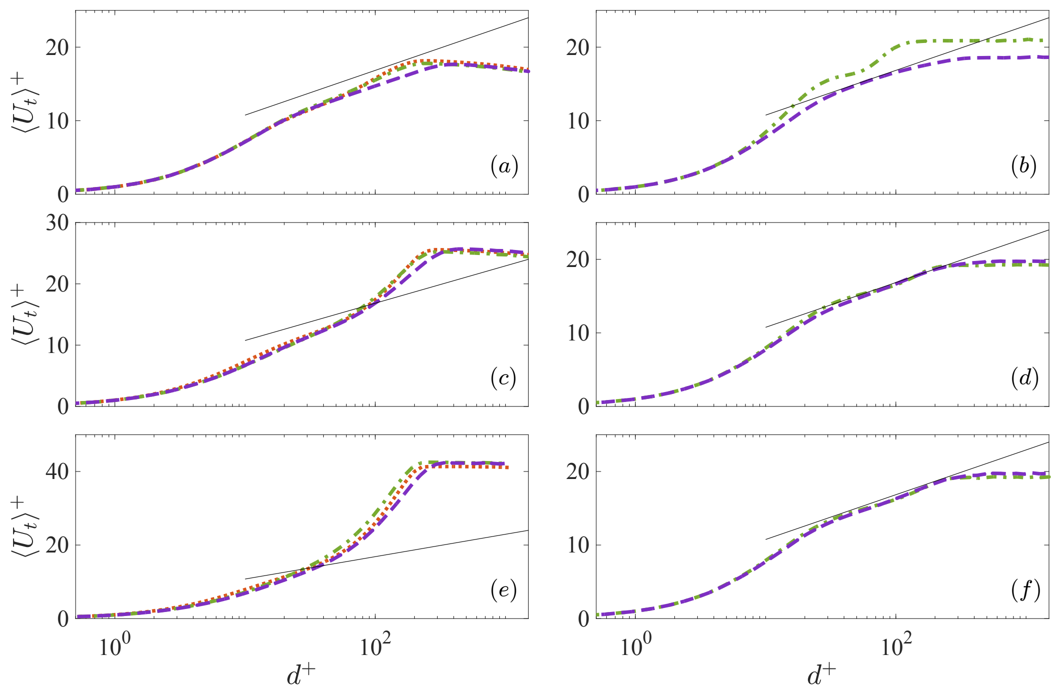

Figure 11. Wall-parallel velocity profiles in wall units for the turbulent cases. $(a, b) : x/c = 0.35$, $(c, d) : x/c = 0.67$, $(e, f) : x/c = 0.82$. (a, c, e) Suction side; (b, d, f) pressure side. TBL; RLE1; RLE2; Thin line: $2.5 \log d^+ + 5$.

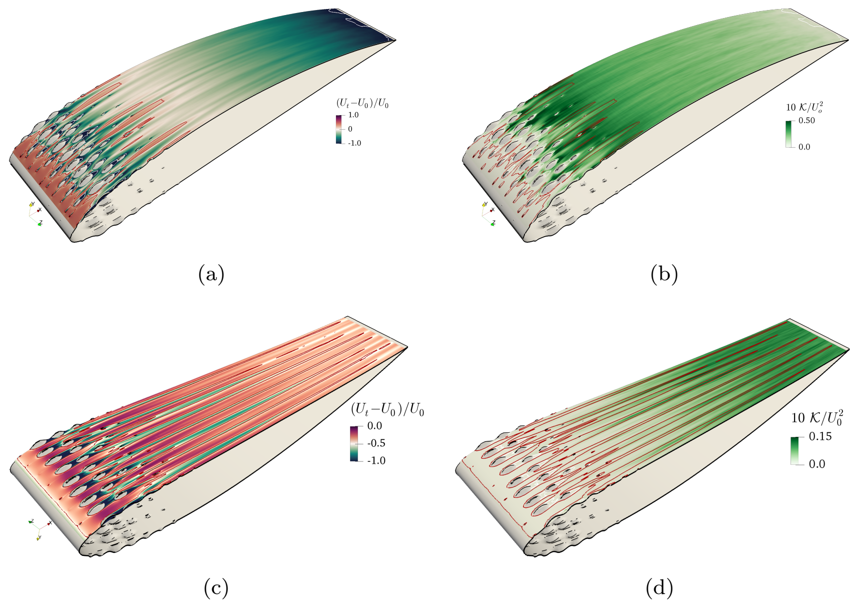

Figure 12. RLE1 case. (a,c) Time-averaged wall-parallel velocity-deficit contours; (b,d) TKE contours. The contours are plotted on a surface at a distance $d/c = 0.002$ from the airfoil. (a,b) Suction side; (c,d) pressure side. The red contour lines represent regions where $U_t = 1.1U_o$ on suction side and $U_t = 0.5U_o$ on pressure side.

shaped structures around 30% of the chord; on the pressure side the flow remains laminar. In the RLE1 case the 3D character of the roughness results in immediate formation of trains of aligned hairpin vortices, on both sides. In the RLE2 case a massive separation behind the roughness is followed by an immediate formation of large hairpin vortices, whose distribution is more random, although some tendency towards the formation of aligned trains can still be observed, especially on the pressure side. These features are reflected in the time-averaged fields for the RLE1 and RLE2 cases (for the TBL case the time-averaged quantities are statistically equal to the double-averaged ones).

Figures 12 & 13 show the normalized mean wall-parallel velocity-deficit, $(U_t - U_o)/U_o$, and the turbulent kinetic energy, $\mathcal{K}/U_o^2$, for the RLE cases. In the RLE1 case the three-dimensionality of the roughness results in the formation of streamwise-oriented, alternating regions of high- and low velocity-fluid, Figure 12(a, c), associated with corresponding regions of low and high TKE. We will term this phenomenon "channelling" and refer to the high velocity streaks as "peak regions", the low-velocity ones as "valley regions". The flow channelling is strongly affected by the pressure gradient; on the pressure side the stabilizing effect of the FPG (which tends to align the vortical structures [92]) the streaks maintain their coherence for longer distances, while the APG on the suction side tends to mix the flow more effectively and break down the streaky structures. For the RLE2 case on the other hand flow channelling, although clearly visible in Figure 13, doesn't look as prominent as RLE1. In fact, due to a closer positioning of roughness elements we see a spanwise ridge like behaviour.

The valley regions are not in the wake of the larger roughness elements. Rather, Figure 14*(a)*, they are formed when the wakes of adjoining elements merge together, and low-speed fluid from the recirculation regions is entrained into the mean flow. The time-averaged data shows pairs of counter-rotating longitudinal vortices, centered on

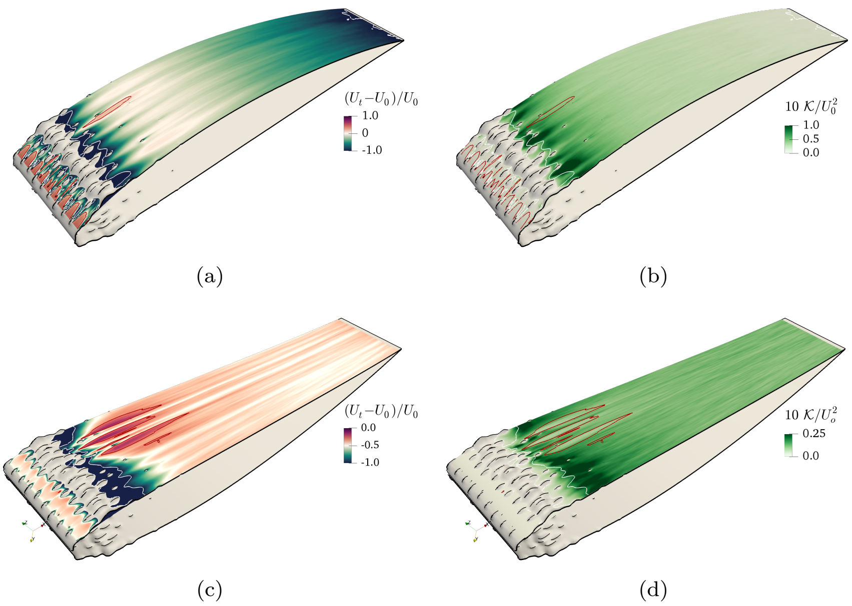

Figure 13. RLE2 case. (a,c) Time-averaged wall-parallel velocity-deficit contours; (b,d) TKE contours. The contours are plotted on a surface at a distance $d/c = 0.002$ from the airfoil. (a,b) Suction side; (c,d) pressure side. The red contour lines represent regions where $U_t = 1.1U_o$ on suction side and $U_t = 0.7U_o$ on the pressure side.

the valley regions and trailing downstream, Figure 14(b); on the pressure side they are remain coherent due to the FPG, but they are also visible on the suction side.

Near the leading edge horseshoe vortices are formed as the flow encounters the first row of roughness elements, which act like isolated obstacles. The legs of the horseshoes trail downstream, meandering in between roughness elements. They remain coherent for the first 20% of the chord on the suction side (longer on the pressure side) and the valleys are the upwash region between the vortices. Towards the end of the roughness region the vortices begin to break down, forming hairpins with lifted heads and shorter, trailing legs. The streamwise vorticity that is present in the time-averaged contours, from this point on, is not due to coherent vortices, but rather to the footprint of the legs of the hairpins that are advected. The alignment of the hairpins observed in Figures 6 and 7 is due to the fact that they originate from the streamwise horseshoe vortices associated with the valleys.

Figure 15 shows the streamwise vorticity in cross planes at $x/c = 0.25$ (note that in the planes shown, the mean flow is almost aligned with the x direction). In the RLE1 case the streamwise vortex pairs are very clear on both sides. In the upwash region between two counter-rotating vortices, the valley regions, the boundary layer is thickened, and the wall stress is decreased.

A similar behaviour can be observed for the RLE2 case, Figure 16. Horseshoe vortices are formed around each roughness element; their trailing legs interact with the horseshoe vortices formed by the next row; this interaction tends to cause the formation of hairpins (*e.g.*, at $x/c \simeq 0.12$ in Figure 16(a)). As in the RLE1 case, the hairpin vortices tend to be aligned with low-speed valley regions, but they are larger and extend further from the wall, probably because of the larger size of the roughness elements. Once the streamwise vortices break down, streamwise vorticity can still be observed; in this case it is the footprint on the time average of the trailing legs of the

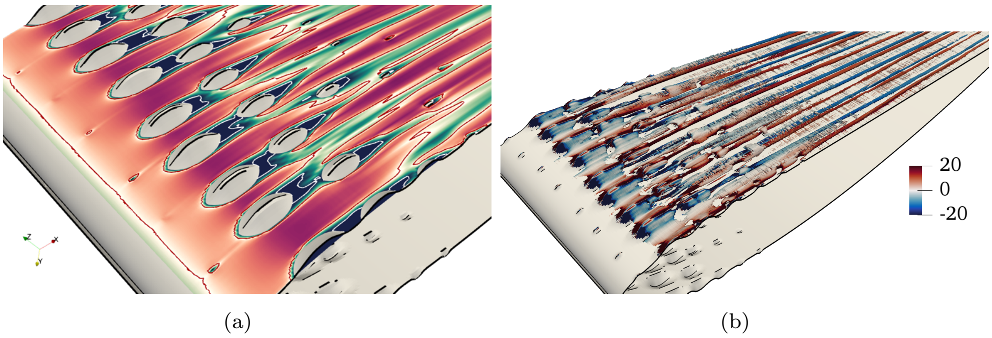

Figure 14. RLE1 case, pressure side. (a) Time-averaged wall-parallel velocity-deficit contours; (green: -1.0, red: 0.0) (b) Iso-surfaces of $\overline{Q} = 20U_o^2/c^2$, coloured by streamwise vorticity, $\Omega_x c/U_o$.

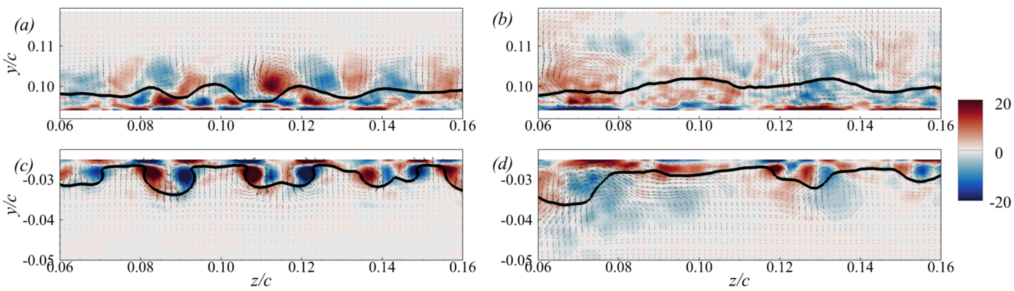

Figure 15. Contours of streamwise vorticity, $\Omega_x c/U_o$, in the $x/c = 0.25$ plane. *(a,b)* Suction side; *(c,d)* pressure side. *(a,c)* RLE1; *(b,d)* RLE2. The solid black lines represent $U_t/U_e = 0.8$.

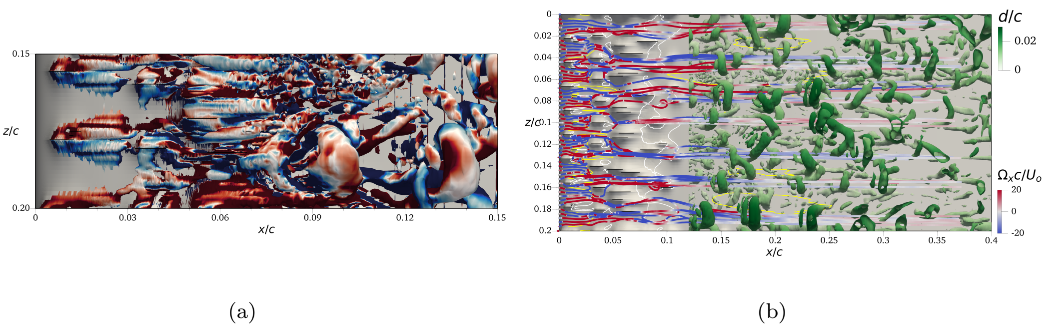

Figure 16. (a) Isosurfaces of Q coloured by instantaneous streamwise vorticity (blue: $-50U_o/c$, red: $50U_o/c$) near the leading edge. (b) Time-averaged streamlines, coloured by streamwise vorticity, $\Omega_x c/U_o$, on the suction side for RLE2 case. Instantaneous structures are also shown after the roughness zone, coloured by distance from the wall d/c. White lines denote separated region and yellow lines denote fast regions on a surface parallel plane at $x/c = 0.002$.

hairpins.

The presence of similar elongated motion in the instantaneous flow-field has been observed by many different studies in standard turbulent boundary layers, both for smooth [93, 94] and rough-wall cases [95, 96]. These regions contribute significantly to TKE and Reynolds shear stresses [97, 98, 99, 100]. Later studies [101, 102, 103, 104] also identified a high degree of spanwise heterogeneity in the mean flow and termed these regions ”low-” and ”high-momentum pathways” (LMPs, HMPs). The flow channelling observed in this study has a similar vortical signature as HMPs and LMPs, but the size of the roughness elements ($h/\delta >> 1$) is much larger than in typical boundary layer studies ($h/\delta \sim 1/20 - 1/40$). The channelling observed here and the vortical structure associated with it have a larger scale, more akin to that of flows in urban environments, although their effects on the mean flow are in many ways similar.

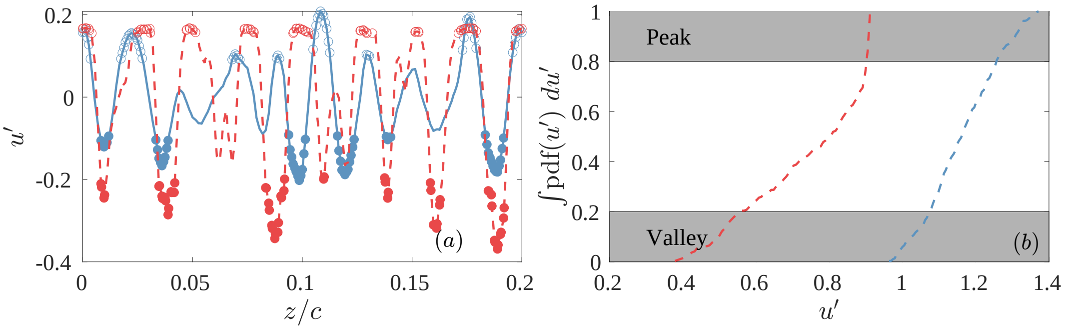

Figure 17. Conditional average threshold choice. *(a)* Profile of u' at $x/c = 0.2$, $d/c = 0.005$; the circles indicate the events identified as ”peaks” (empty) and ”valleys” (filled). *(b)* Cumulative pdf of u'. ▬▬ Suction side; - - - pressure side.

3.6. Conditional and phase averaging

Figures 12 and 13 show that both in RLE1 and RLE2 cases the high-speed peak regions are accompanied by lower levels of TKE. To understand better this behaviour, and its possible implications on flow physics and modelling, we performed conditional averages of the time-averaged quantities in peak and valley regions. The peaks and valleys were identified by considering a spanwise profile of the $\Delta U = U - \langle U \rangle$, at $x/c = 0.2$ and $d/c = 0.005$, shown in Figure 17*(a)*. The cumulative probability-density function (CPDF), shown in Figure 17*(b)*, was calculated, and the events responsible for the top and bottom 20% of the CPDF were classified as “peaks” and “valleys”, respectively. They are shown as empty and full circles in the Figure. The average over all peak or valley events will be denoted by a hat: $\widehat{U}$.

The conditionally averaged result on the suction side, for RLE1 and RLE2 cases are shown in Figure 18, and compared with the double-averaged velocity. Significant differences between the flow statistics are observed. First, the friction velocity is approximately 12% lower than the DA one in the valley regions, and higher in the peak regions by 3% (for the RLE2 case) or 7% (for RLE1). Furthermore, in the valley regions, the wake region is more pronounced and the velocity profiles resemble those in boundary layers with adverse pressure gradient (APG), Figures 18*(a,b)*. Conversely, in the peak regions the behaviour tends towards that of a boundary layer in favourable pressure gradient (FPG), with a slight increase of the von Kàrmàn constant and the disappearance of the wake region. In outer units, the velocity difference between peak

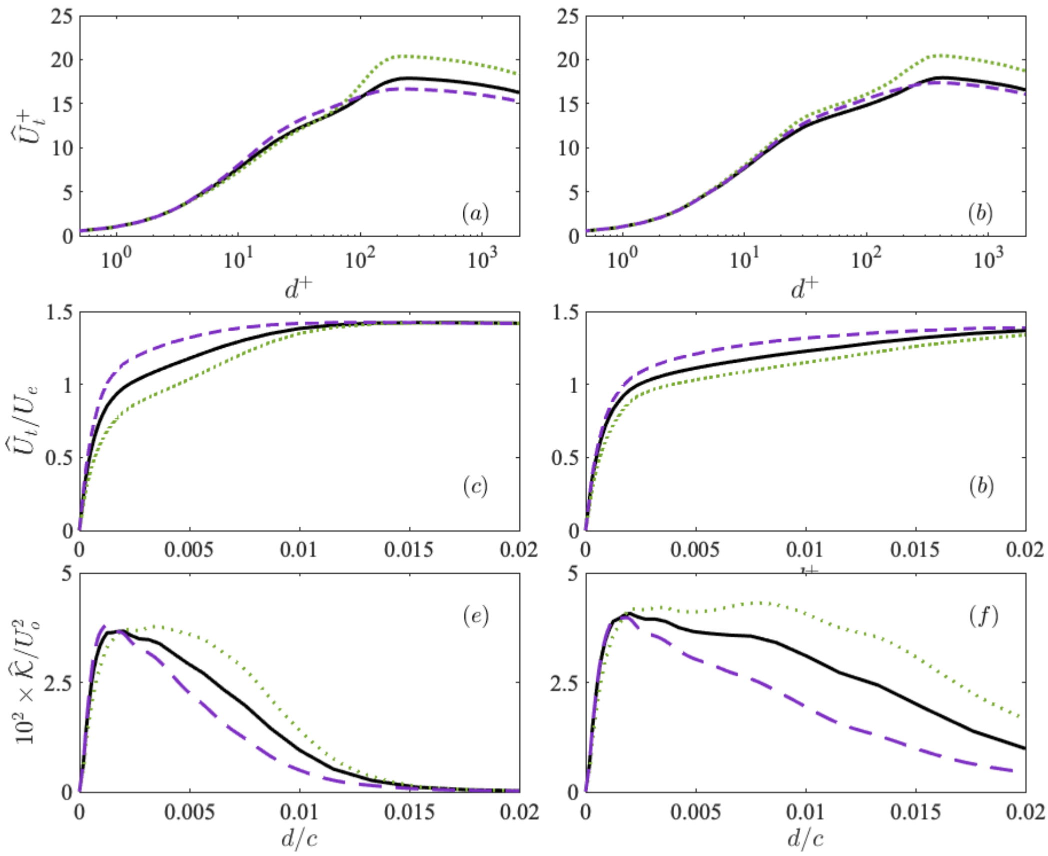

Figure 18. Conditionally averaged tangential velocity and turbulent kinetic energy (in outer coordinates) in peak and valley regions. x/c = 0.25. *(a,c,e)* RLE1; *(b,d,f)* RLE2; *(a,b)* tangential velocity in wall units; *(c,d)* tangential velocity in outer coordinates; *(e,f)* turbulent kinetic energy in outer coordinates. ▬▬ Double average; ···· Valley; - - - Peak.

and valley regions can be as high as 30% of the edge velocity in the RLE1 case, 18% in the RLE2 case, Figures 18*(c,d)*. In the valley regions the velocity profile has inflection points in both cases, although less marked in the RLE2 case. These inflection points may be responsible for the significant increase of the TKE in the valley regions, Figure 18*(d,e)*. The increased TKE in the valleys and, conversely, the increased one in the peak regions, are also consistent with the APG-FPG behaviour of these regions. By $x/c = 0.4$ the differences between valley and peak regions are not significant any longer. The peak/valley behaviour is similar on the pressure side (not shown), although the differences are more marked (especially the inflectional behaviour of the tangential velocity) and persist farther downstream.

4. Conclusions

We performed large-eddy simulations of the flow over the NACA4412 airfoil at $Re = 200,000$ and 5^o angle of attack to study the effect of leading-edge ice deposits on the turbulent flow. Four cases were considered: an airfoil with a smooth leading edge (SLE), one with a tripped leading edge (TLE) with 3 semi-cylindrical bars aligned in the z-direction, and two cases with Rough Leading-Edges (RLE1 and RLE2) to mimic the glaze icing described in the study of McClain *et al.* [29]. A grid-convergence study was performed for TBL case; three grids were chosen: coarse, medium and fine. The first-order statistics converge using the medium resolution; the convergence of second-order moments is marginal, but within acceptable bounds.

Statistical quantities and instantaneous flow visualizations were computed. The triple decomposition introduced for rough-wall flows [79, 80] was used to distinguish the double-averaged quantities (averaged over time and the spanwise direction) from the time-averaged ones. Conditional averages were also performed to isolate the flow in the peak and valley regions.

In the SLE case the laminar flow separates, and transition is caused by the instability of the separated shear layer. Two-dimensional vortices are formed after reattachment, which develop three-dimensionalities; eventually, the flow becomes turbulent around the middle of the airfoil.

The main effect of the leading-edge roughness is to accelerate the transition to turbulence. In the TBL cases transition occurs much earlier. The separated flow over the semi-cilindrical trips causes the formation of quasi two-dimensional spanwise vortices. The remain 2D for 20-30% of the chord, then 3D structures are formed and the flow becomes more chaotic.

A very three-dimensional flow is established immediately in the RLE1 and RLE2 cases. In the first, in which the roughness elements are separated, their wakes merge and low- and high-speed streaks are formed; they are referred to “valley” and “peak” regions, respectively. We refer to this phenomenon as “channelling”. Horseshoe vortices are initially formed after each roughness element; the trailing legs interact with those of of successive roughness elements and eventually break down, giving rise to trains of hairpin vortices, aligned with the low-speed streaks. In the mean field, both the horseshow legs and the hairpin legs result in coherent and fairly stationary streamwise-vorticity regions. In the upwash region between the hairpin legs the boundary layer is thickened, the wall stress is lower than the average, and low-speed streaks are formed. The flow in the valley regions resembles that in an APG boundary layer: the conditionally averaged velocity profiles exhibits a more considerable wake and inflection points. As a consequence, turbulent kinetic energy and Reynolds stresses are significantly larger in the valley regions. In the peak regions, conversely, the flow appears more similar to an FPG boundary layer. The channelling is amplified by the favourable pressure gradient on the lower side of the airfoil, where the streaks last much longer, and the streamwise vortices remain more coherent.

In the RLE2 case the largest roughness elements merge together, forming a ridge. The channelling phenomenon is less clear, but still present. Peaks and valleys are still observed, and show similar characteristics. the hairpin vortices are larger, extend further from the surface and meander more.

The channelling is similar to that observed in other rough wall flows [103], but the particular geometry considered, with more isolated roughness elements than in more conventional rough-wall boundary layers, affects its features significantly. It may be the most interesting finding of this work, also because of its implications for modelling. In industrial applications, calculations of the flow over an entire wing are typically performed solving the Reynolds-Averaged Navier-Stokes (RANS) equations with turbulence models. They use grid spacings of order $0.01 - 0.02c$; in rare cases finer grids are used. In our calculations the roughness size was less than $0.01c$, and the spacing between consecutive high- or low-speed regions is of order $0.025c$. None of these geometric characteristics would be resolved on a typical grid. The roughness, therefore, would have to be included through a modification of the turbulence model. Several such modifications have been developed (see, for instance, the discussion in [105]).

They are all based on statistical considerations, and a single parameter (generally the equivalent sandgrain roughness) is used to describe the roughness. Such approach cannot distinguish between the various mechanisms associated with the geometries considered here, however, yielding only the equivalent of the double-averaged statistics. Moreover, it would not be able to account for the channelling phenomenon, which may play a role at high angles of attack, causing three-dimensional separation. In fully turbulent flows, roughness generally causes the flow to separate earlier; the APG in the valley regions might further accelerate separation, resulting in a very 3D structure of the separated-flow region. It is unclear if this phenomenon could be captured at all by a Reynolds-Averaged Navier-Stokes solution.

The present simulations were carried out at a moderate Reynolds number, and it is possible that some of the problems described lose importance if the Reynolds number is increased. It should be remarked, however, that the dimensions of the three-dimensional structures observed here scale with geometric parameters (the roughness size) and not in viscous units. It is, therefore, unlikely that the phenomena observed would entirely disappear in flight conditions. It would be, however, desirable to verify this conjecture by performing simulations at higher Reynolds number and angle of attack. These calculations would also help determine the error bars for the turbulence models used in these configurations.

Acknowledgments

VK acknowledges the financial support by Mitacs, Bombardier Aerospace and CARIC/CRIAQ. UP acknowledges the support from the Natural Science and Engineering Research Council of Canada (NSERC) under the Discovery Grant program, and the Canada Research Chair program. This research was enabled in part by computational support provided by Compute Ontario (computeontario.ca) and Southern Ontario Smart Computing Innovation Platform (SOSCIP) (www.soscip.org).

References

[1] G. K. Faust and P. Mangur. Status report on a natural laminar-flow nacelle flight experiment - nacelle design. NASA Technical Report N90-12550, NASA, 1987.

[2] C. J. Obara and S. S. Dodbele. Nacelle aerodynamic performance. NASA Technical Report N90-12552, NASA, 1987.

[3] R. W. Gent, N. P. Dart, and J. T. Cansdale. Aircraft icing. Phil. Trans. Roy. Soc. A, 358(1776):2873–2911, 2000.

[4] T. Cebeci and F. Kafyeke. Aircraft icing. Ann. Rev. Fluid Mech., 35(1):11–21, 2003.

[5] R. J. Shaw. Progress toward the development of an aircraft icing analysis capability. NASA Technical Memorandum TM-83562, NASA, 1984.

[6] R. J. Shaw. NASA's aircraft icing analysis program. NASA Technical Memorandum TM-88791, NASA, Cleceland, Ohio, 1984.

[7] D. Guffond, J. Cassaing, and L. Brunet. Overview of icing research at ONERA. In 23rd Aerospace Sciences Meeting, Reston, Virigina, jan 1985. AIAA J.

[8] T. Hedde and D. Guffond. ONERA three-dimensional icing model. AIAA J., 33(6):1038–1045, 1995.

[9] M. M. Oleskiw. A review of 65 years of aircraft in-flight icing research at NRC. Can. Aeronaut. Space J., 47(3):259–268, 2001.
[10] G. A. Isaac, S. G. Cober, J. W. Strapp, A. V. Korolev, A. Tremblay, and D. L. Marcotte. Recent Canadian research on aircraft in-flight icing. Can. Aeronaut. Space J., 47(3):213–221, 2001.
[11] W. B. Wright, P. Struk, T. Bartkus, and G. Addy. Recent advances in the lewice icing model. 2015.
[12] W. Wright, M. Potapczuk, and L. Levinson. Comparison of lewice and glennice in the sld regime. In 46th AIAA Aerospace Sciences Meeting and Exhibit, page 439, 2008.
[13] R. Hann. Uav icing: Comparison of lewice and fensap-ice for ice accretion and performance degradation. In 2018 Atmospheric and Space Environments Conference, page 2861, 2018.
[14] Richard Hann. Uav icing: Comparison of lewice and fensap-ice for anti-icing loads. In AIAA Scitech 2019 Forum, page 1286, 2019.
[15] Héloïse Beaugendre, Pascal Benquet, Wagdi G. Habashi, and François Morency. Roughness Implementation in FENSAP-ICE: Model Calibration and Influence on Ice Shapes. J. Aircr., 40(6):1212–1215, 2003.
[16] Giulio Croce, Erika De Candido, Wagdi G. Habashi, Jeffrey Munzar, Martin S. Aubé, Guido S. Baruzzi, and Cristhian Aliaga. FENSAP-ICE: Analytical model for spatial and temporal evolution of in-flight icing roughness. J. Aircr., 47(4):1283–1289, 2010.
[17] S. Zhang, O. El Kerdi, R. A. Khurram, and W. G. Habashi. FEM analysis of in-flight ice break-up. Finite Elem. Anal. Des., 57:55–66, 2012.
[18] R. Jones and D. H. Williams. Effect of surface roughness on characteristics of aerofoils NACA 0012 and RAF 34. ARC Technical Report TR-2264, ARC, 1936.
[19] E. N. Jacobs. Airfoil section characteristics as affacted by protuberances. NACA Technical Report TR-446, NACA, 1932.
[20] T. Cebeci. Effects of environmentally on airfoil imposed roughness performance. NASA Contractor Report CR-179639, NASA, 1987.
[21] T. Cebeci. Calculation of flow over iced airfoils. AIAA J., 27(7):853–861, 1989.
[22] F. T. Lynch and A. Khodadoust. Effects of ice accretions on aircraft aerodynamics. Prog. Aero. Sci., 37(8):669–767, 2001.
[23] M. B. Bragg, A. P. Broeren, and L. A. Blumenthal. Iced-airfoil aerodynamics. Prog. Aero. Sci., 41(5):323–362, 2005.
[24] J. Shin, H. Chen, and T. Cebeci. A turbulence model for iced airfoils and its validation. *AIAA Paper 1992-417*, 1992.
[25] J. Shin, B. Berkowitz, H. H. Chen, and T. Cebeci. Prediction of ice shapes and their effect on airfoil drag. J. Aircraft, 31(2):263–270, 1994.
[26] J. Shin. Characteristics of surface roughness associated with leading-edge ice accretion. J. Aircraft, 33(2):316–21, 1996.
[27] D. Anderson and J. Shin. Characterization of ice roughness from simulated icing encounters. *AIAA Paper 97-0052*, 1 1997.
[28] S.T. McClain, D. Reed, M. Vargas, R. E. Kreeger, and J. C. Tsao. Ice roughness in short duration SLD icing events. *AIAA Paper 2014-2330*, 2014.
[29] S. T. McClain, M. Vargas, and J. C. Tsao. Characterization of ice roughness variations in scaled glaze icing conditions. *AIAA Paper 2016-3592*, 2016.
[30] S. T. McClain, M. Vargas, J.C. Tsao, A.P. Broeren, and S. Lee. Ice accretion roughness measurements and modeling. In *7th European conference for aeronautics and space sciences (EUCASS)*, 2017.

[31] S. T. McClain, M. Vargas, and J.-C. Tsao. Characterization of ice roughness variations in scaled glaze icing conditions. *AIAA Paper 2017-0244*, 2017.
[32] Ralph E Brumby. Wing surface roughness: Cause and effect. DC Flight Approach, 32:2–7, 1979.
[33] RE Brumby. The effect of wing ice contamination on essential flight characteristics. In AGARD Conference Proceedings, number 496, 1991.
[34] Y. Han, J. Palacios, and S. Schmitz. Scaled ice accretion experiments on a rotating wind turbine blade. J. Wind. Eng. Ind. Aerodyn., 109:55–67, 2012.
[35] V. H. Gray and U. H. von Glahn. Aerodynamic effects caused by icing of an unswept naca65a004 airfoil. 1958.
[36] W. J. Jasinski, S. C. Noe, M. S. Selig, and M. B. Bragg. Wind turbine performance under icing conditions. 1998.
[37] M. F. Kerho and M. B. Bragg. Airfoil boundary-layer development and transition with large leading-edge roughness. AIAA J., 35(1):75–84, 1997.
[38] M. J. Cummings and M. B. Bragg. Boundary layer transition due to isolated three-dimensional roughness on airfoil leading edge. AIAA J., 34(9):1949–1952, sep 1996.
[39] B. Plogmann, W. Wurz, and E. Krämer. Interaction of a laminar boundary layer with a cylindrical roughness element near an airfoil leading edge. *AIAA Paper 2012-3077*, 2012.
[40] Y. Zhang, T. Igarashi, and H. Hu. Experimental Investigations on the Performance Degradation of a Low-Reynolds-Number Airfoil with Distributed Leading Edge Roughness. In 49th AIAA Aerospace Sciences Meeting including the New Horizons Forum and Aerospace Exposition, number January, pages 1–18, Reston, Virigina, jan 2011. AIAA.
[41] Y. Zhang. Effects of distributed leading-edge roughness on aerodynamic performance of a low-Reynolds-number airfoil: An experimental study. Theoret. Appl. Mech. Lett., 8(3):201–207, 2018.
[42] A. M. O. Smith and Kalle Kaups. Aerodynamics of Surface Roughness and Imperfections. In SAE Technical Papers, feb 1968.
[43] M. B. Bragg. Predicting airfoil performance with rime and glazed ice accretion. *AIAA Paper AIAA-84-0106*, 1984.
[44] D. T. Bowden. Effect of pneumatic de-icers and ice formations on aerodynamic characteristics of an airfoil. NACA Technical Note TN-3564, NACA, 1956.
[45] M Bragg and G Gregorek. Environmentally induced surface roughness effects on laminar flow airfoils-implications for flight safety. In Aircraft Design and Operations Meeting, page 2049, 1989.
[46] D. G. Jackson. Effect of simulated ice and residual ice roughness on the performance of a natural laminar flow airfoil. PhD thesis, University of Illinois at Urbana-Champaign, 1999.
[47] M. K. Vinnes and R. J. Hearst. Aerodynamics of an airfoil with leading-edge icing. Wind Energy, pages 1–17, 2020.
[48] C. M. Brown, R. F. Kunz, M. P. Kinzel, J. W. Lindau, J. L. Palacios, and K. S. Brentner. Large eddy simulation of airfoil ice accretion aerodynamics, 2014.
[49] S. J. Stebbins, E. Loth, A. P. Broeren, and M. Potapczuk. Review of computational methods for aerodynamic analysis of iced lifting surfaces. Prog. Aerosp. Sci., 111:100583–1–28, 2019.
[50] D. Thompson, P. Mogili, S. Chalasani, H. Addy, and Y. Choo. A computational icing effects study for a three-dimensional wing. In 42nd AIAA Aerospace Sciences Meeting and Exhibit, page 561, 2004.

[51] X Chi, B Williams, N Crist, Richard Kreeger, Richard Hindman, and Tom Shih. 2-d and 3-d cfd simulations of a clean and an iced wing. In 44th AIAA Aerospace Sciences Meeting and Exhibit, page 1267, 2006.

[52] Kyle Chi, Brandon Williams, Richard Kreeger, Richard Hindman, and Tom Shih. Simulations of finite wings with 2-d and 3-d ice shapes: Modern lifting-line theory versus 3-d cfd. In 45th AIAA Aerospace Sciences Meeting and Exhibit, page 504, 2007.

[53] M. Alam, K. Walters, and D. Thompson. Simulations of separated flow around an airfoil with ice shape using hybrid rans/les models. In 29th AIAA Applied Aerodynamics Conference, page 3972, 2011.

[54] C. Butler, C. Qin, and E. Loth. Improved delayed detached-eddy simulation on a swept hybrid model in irt. In 8th AIAA atmospheric and space environments conference, page 3736, 2016.

[55] E. S. Oztekin and J. T. Riley. Ice accretion on a naca 23012 airfoil. In 2018 Atmospheric and Space Environments Conference, page 2860, 2018.

[56] Maochao Xiao, Yufei Zhang, and Feng Zhou. Numerical study of iced airfoils with horn features using large-eddy simulation. J. Aircraft, 56(1):94–107, 2019.

[57] B. König, E. Fares, and A. P. Broeren. Lattice-boltzmann analysis of three-dimensional ice shapes on a naca 23012 airfoil. Technical report, SAE Technical Paper, 2015.

[58] A.F.P. Ribeiro, B. Konig, and E. Fares. On the Stall Characteristics of Iced Wings. In 55th AIAA Aerospace Sciences Meeting, number January, pages 1–10, Reston, Virginia, jan 2017. American Institute of Aeronautics and Astronautics.

[59] A. Ribeiro, D. Casalino, E. Fares, and M. Choudhari. Direct numerical simulation of an airfoil with sand grain roughness on the leading edge. NASA Technical Memorandum TM 219363, NASA, 2016.

[60] A F P Ribeiro, E Fares, and M Choudhari. DNS of laminar to turbulent transition on NACA0012 airfoil with sand grain roughness. In *Tenth International Conference on ICCFD10-xxxx Computational Fluid Dynamics (ICCFD10)*, 2018.

[61] U. Piomelli, A. Rouhi, and B. J. Geurts. A grid-independent length scale for large-eddy simulations. J. Fluid Mech., 766:499–527, 2015.

[62] A. Rouhi, U. Piomelli, and B. J. Geurts. A dynamic subfilter-scale stress model for large eddy simulations. Phys. Rev. Fluids, 1(4):044401–1–26, 2016.

[63] O. Lehmkuhl, U. Piomelli, and G. Hozeaux. On the extension of the integral length-scale approximation model to complex geometries. Int. J. Heat Fluid Flow, 78(108422):1–12, 2019.

[64] M. Vázquez, G. Houzeaux, S. Koric, A. Artigues, J. Aguado-Sierra, R. AríS, D. Mira, H. Calmet, F. Cucchietti, H. Owen, A. Taha, E. D. Burness, J. M. Cela, and M. Valero. Alya: Multiphysics engineering simulation toward exascale. J. Comput. Sci., 14:15–27, 5 2016.

[65] G. Houzeaux, M. Vázquez, R. Aubry, and J. M. Cela. A massively parallel fractional step solver for incompressible flows. J. Comput. Phys., 228(17):6316–6332, 2009.

[66] S. Gövert, D. Mira, J.B.W. Kok, M. Vázquez, and G. Houzeaux. Turbulent combustion modelling of a confined premixed jet flame including heat loss effects using tabulated chemistry. Appl. Energy, 156:804–815, 10 2015.

[67] S. Gövert, D. Mira, M. Zavala-Ake, J.B.W. Kok, M. VáZquez, and G. Houzeaux. Heat loss prediction of a confined premixed jet flame using a conjugate heat transfer approach. Int. J. Heat Mass Transf., 107:882–894, 4 2017.

[68] I. Rodríguez, G. Borell, O. Lehmkuhl, and C. D. Perez-Segarra. Direct numerical simulation of the flow over a sphere at $re = 3700$. J. Fluid Mech., 679:263–287, 2011.
[69] D. E. Aljure, O. Lehmkuhl, I. Rodríguez, and A. Oliva. Flow and turbulent structures around simplified car models. Comput. Fluids, 96:122–135, 2014.
[70] O. Lehmkuhl, A. Lozano-Durán, and I. Rodríguez. Active flow control for external aerodynamics: from micro air vehicles to a full aircraft in stall. J. Phys.: Conf. Series, 1522(012017):1–15, 2020.
[71] Sergey Charnyi, Timo Heister, Maxim A. Olshanskii, and Leo G. Rebholz. On conservation laws of Navier-Stokes Galerkin discretizations . J. Comput. Phys., 337:289 – 308, 2017.
[72] F. X. Trias and O. Lehmkuhl. A self-adaptive strategy for the time integration of Navier-Stokes equations. Num. Heat Transf. B, 60(2):116–134, 2011.
[73] O. Lehmkuhl, G. Houzeaux, H. Owen, G. Chrysokentis, and I. Rodriguez. A low-dissipation finite element scheme for scale resolving simulations of turbulent flows. J. Comput. Phys., 390:51 – 65, 2019.
[74] Rainald Lohner, Fernando Mut, Juan Raul Cebral, Romain Aubry, and Guillaume Houzeaux. Deflated preconditioned conjugate gradient solvers for the pressure-poisson equation: Extensions and improvements. Int. J. Numer. Methods Eng., 87(1â5):2–14, 2011.
[75] O. Lehmkuhl, A. Baez, I. Rodríguez, and C. D. Pérez-Segarra. Direct numerical simulation and large-eddy simulations of the turbulent flow around a NACA-0012 airfoil. In 7th International Conference on Computational Heat and Mass Transfer, 2011.
[76] A. Baez, O. Lehmkuhl, I. Rodríguez, and C. D. Perez-Segarra. Direct numerical simulation of the turbulent flow around a NACA0012 airfoil at different angles of attack. In *Parallel CFD 2011*, 2011.
[77] Christophe Geuzaine and Jean François Remacle. Gmsh: A 3-D finite element mesh generator with built-in pre- and post-processing facilities. Int. J. Numer. Methods Eng., 2009.
[78] Ricardo Vinuesa, Prabal Singh Negi, M Atzori, Ardeshir Hanifi, Dan S Henningson, and Philipp Schlatter. Turbulent boundary layers around wing sections up to rec= 1,000,000. Int. J. Heat Fluid Flow, 72:86–99, 2018.
[79] V. Nikora, I. McEwan, S. McLean, S. Coleman, D. Pokrajac, and R. Walters. Double-averaging concept for rough-bed open-channel and overland flows: theoretical background. J. Hydr. Engng, 133(8):873–883, 2007.
[80] E. Mignot, E. Barthelemy, and D. Hurter. Double-averaging analysis and local flow characterization of near-bed turbulence in gravel-bed channel flows. J. Fluid Mech., 618:279—303, 2009.
[81] F. Mallor. Enabling high-fidelity measurements of turbulent boundary layer flow over wing sections in the MTL wind tunnel. PhD thesis, KTH, Stockholm, Sweden, 2019.
[82] L. P. Erm and P. N. Joubert. Low-Reynolds-number turbulent boundary layers. J. Fluid Mech., 230:1–44, 9 1991.
[83] P. Schlatter and R. Örlü. Turbulent boundary layers at moderate reynolds numbers: inflow length and tripping effects. J. Fluid Mech., 710:5–34, 11 2012.
[84] A. Tanarro, F. Mallor, N. Offermans, A. Peplinski, R. Vinuesa, and P. Schlatter. Enabling adaptive mesh refinement for spectral-element simulations of turbulence around wing sections. Flow, Turb. Comb., 105(2):415–436, 8 2020.
[85] O. Lehmkuhl, I. Rodríguez, A. Baez, A. Oliva, and C. D. Pérez-Segarra. On the

large-eddy simulations for the flow around aerodynamic profiles using unstructured grids. Comp. Fluids, 84:176–189, 9 2013.

[86] T. B. Nickels. Inner scaling for wall-bounded flows subject to large pressure gradients. J. Fluid Mech., 521:217–239, 12 2004.

[87] K. A. Chauhan, P. A. Monkewitz, and H. M. Nagib. Criteria for assessing experiments in zero pressure gradient boundary layers. Fluid Dyn. Res., 41(2):021404, 4 2009.

[88] P. Li, Q.And Schlatter, L. Brandt, and D. S. Henningson. DNS of a spatially developing turbulent boundary layer with passive scalar transport. Int. J. Heat Fluid Flow, 30(5):916–929, 10 2009.

[89] P. R. Spalart and J. H. Watmuff. Experimental and numerical study of a turbulent boundary layer with pressure gradients. J. Fluid Mech., 249:337–371, 1993.

[90] R. Vinuesa, A. Bobke, R. Örlü, and P. Schlatter. On determining characteristic length scales in pressure-gradient turbulent boundary layers. Phys. Fluids, 28:1–13, 2016.

[91] K. P. Griffin, L. Fu, and P. Moin. General method for determining the boundary-layer thickness in non-equilibrium flows. Phys. Rev. Fluids, 6:024608, 2021.

[92] U. Piomelli and J. Yuan. Numerical simulations of spatially developing, accelerating boundary layers. Phys. Fluids, 25:101304–1—21, 2013.

[93] R. J. Adrian, C. D. Meinhart, and C. D. Tomkins. Vortex organization in the outer region of the turbulent boundary layer. J. Fluid Mech., 422:1–54, 2000.

[94] C. D. Tomkins and R. J. Adrian. Spanwise structure and scale growth in turbulent boundary layers. J. of Fluid Mech., 490(490):37–74, 2003.

[95] R. J. Volino, M. P. Schultz, and K. a. Flack. Turbulence structure in rough- and smooth-wall boundary layers. J. Fluid Mech., 592:263–293, 2007.

[96] Y Wu and K T Christensen. Outer-layer similarity in the presence of a practical rough-wall topography. Phys. Fluids, 19(8):85108, 2007.

[97] Bharathram Ganapathisubramani, Ellen K. Longmire, and Ivan Marusic. Characteristics of vortex packets in turbulent boundary layers. J. of Fluid Mech., 478(478):35–46, 2003.

[98] V. K. Natrajan and K. T. Christensen. The role of coherent structures in subgrid-scale energy transfer within the log layer of wall turbulence. Phys. Fluids, 18(6), 2006.

[99] N. Hutchins and Ivan Marusic. Evidence of very long meandering features in the logarithmic region of turbulent boundary layers. J. Fluid Mech., 579:1–28, 2007.

[100] Y. Wu and K. T. Christensen. Spatial structure of a turbulent boundary layer with irregular surface roughness. J. Fluid Mech., 655:380–418, 2010.

[101] B. Nugroho, N. Hutchins, and J. P. Monty. Large-scale spanwise periodicity in a turbulent boundary layer induced by highly ordered and directional surface roughness. Int. J. Heat Fluid Flow, 41:90–102, 2013.

[102] R. Mejia-Alvarez and K. T. Christensen. Wall-parallel stereo particle-image velocimetry measurements in the roughness sublayer of turbulent flow overlying highly irregular roughness. Phys. Fluids, 25(11), 2013.

[103] Julio M. Barros and Kenneth T. Christensen. Observations of turbulent secondary flows in a rough-wall boundary layer. J. Fluid Mech., 748:R1, 2014.

[104] David Willingham, William Anderson, Kenneth T. Christensen, and Julio M. Barros. Turbulent boundary layer flow over transverse aerodynamic roughness transitions: Induced mixing and flow characterization. Phys. Fluids, 26(2), 2014.

[105] R. Dutta, J. Nicolle, A.-M. Giroux, and U. Piomelli. Evaluation of turbulence models in rough-wall boundary layers for hydroelectric application. Int. J. Fluid Mach. Sys., 10(3):228–239, 2017.